Supplementary information: In-silico molecular enrichment and clearance of the human intracranial space

Marius Causemann[1], **Miroslav Kuchta**[1], **Rami Masri**[2], **and Marie E. Rognes** [1,3,*]

[1]Department of Numerical Analysis and Scientific Computing, Simula Research Laboratory, Oslo, Norway
[2]Division of Applied Mathematics, Brown University, Providence, Rhode Island, USA
[3]K. G. Jebsen Centre for Brain Fluid Research, University of Oslo, Norway
[*]meg@simula.no

ABSTRACT

Supplementary methods and discussion accompanying the main text of *In-silico molecular enrichment and clearance of the human intracranial space*.

S1 Supplementary methods

These sections provide more detailed descriptions of the mathematical models and numerical approximations considered.

S1.1 Mixed-dimensional transport and flow equations

S1.1.1 Notation

In terms of geometrical domains, we consider the parenchyma $\Omega_{\text{PAR}} \subset \mathbb{R}^3$ and CSF spaces $\Omega_{\text{CSF}} \subset \mathbb{R}^3$ with $\Omega = \Omega_{\text{PAR}} \cup \Omega_{\text{CSF}}$ (Fig. 1A, Fig. 2A–C). The coordinates in these 3D domains is denoted by x. The interface between the parenchyma and CSF spaces is given by $\partial\Omega_{\text{PAR}} \cap \partial\Omega_{\text{CSF}}$ and we separate it as two parts: the surface of the lateral ventricles Γ_{LV} and the remaining pial interface Γ_{pia} (thus $\partial\Omega_{\text{CSF}} \bigcap \partial\Omega_{\text{PAR}} = \Gamma_{\text{LV}} \cup \Gamma_{\text{pia}}$). The remaining, outer, boundary of Ω_{CSF} is again separated into two parts: Γ_{SSAS} represents the lower interface towards the spinal subarachnoid space (SSAS), while Γ_{AM} is the outer interface towards the arachnoid and dura membranes. Γ_{AM} is further subdivided into its lower and upper parts: $\Gamma_{\text{AM-L}}$ and $\Gamma_{\text{AM-U}}$. The boundary towards the spinal cord is denoted by Γ_{SC} and given by $\Gamma_{\text{SC}} = \partial\Omega_{\text{PAR}} \setminus \partial\Omega_{\text{CSF}}$.

In addition, we consider two sets of perivascular networks: a periarterial network Λ_a represented by the (connected) centerlines Λ_a^i of the arterial tree, and a perivenous network Λ_v associated with the centerlines Λ_v^i of the veins. Recall that we represent the vascular domains as the union of cylindrical vessels of radius R_1^i surrounding the centerlines Λ^i. Moreover, we consider the surrounding perivascular spaces as the union of annular cylinders Ω^i of inner radius R_1^i and outer radius $R_2^i > R_1^i$ and thus of width $R_2^i - R_1^i$, and remark that we interpret R_2^i and R_1^i as temporal averages (fixed in time), as the pulsations considered in Section S1.4 are beyond the temporal resolution of our model. We denote the outer lateral surface of the periarterial and perivenous spaces by Γ_a and Γ_v, respectively. We omit the subscript a or v when referring to any such network, vessel segment or perivascular outer surface. We assume that Λ is parametrized by the coordinate s, and with a minor abuse of notation, simply write $s \in \Lambda$ to represent the point $\boldsymbol{\lambda}(s)$ on Λ corresponding to s. Finally, we view each perivascular network both as a geometric domain and as a directed graph with the centerlines $\{\Lambda^i\}$ as oriented edges and the connections as nodes $\mathcal{V}$.

S1.1.2 Solute transport and exchange in intracranial domains (3D) and perivascular networks (1D)

In this section, we describe the mathematical model (eq. (1)), the associated definitions, interface and boundary conditions in further detail. We refer to the main text for explicit parameter values while giving the general, abstract form here, and to the reference[1,2] for the derivation and analysis of this 3D-1D model. Recall that we model a concentration field $c = c(x,t)$ for $x \in \Omega$ and $t > 0$ defined in Ω_{PAR} and Ω_{CSF} separately. In each of these domains, c satisfies

$$\partial_t(\phi c) - \nabla \cdot (D\nabla(\phi c)) + \nabla \cdot (\boldsymbol{u} c) + \xi(\overline{c} - \hat{c})\delta_\Gamma = 0 \qquad \text{in} \quad \Omega_{\text{CSF}}, \Omega_{\text{PAR}}. \tag{1}$$

In (1), ϕ is the fluid volume fraction (also known as the porosity) defined in the parenchyma ($\phi \ll 1$ in Ω_{PAR}) and in the CSF spaces ($\phi = 1$ in Ω_{CSF}). In the parenchyma, ϕ represents the extracellular space volume fraction, and thus c here generally represents the intrinsic (in contrast to the superficial) concentration[3]. Moreover, D is the effective diffusion coefficient of the

relevant solute in the respective media which takes different values over the CSF spaces and the parenchyma, depending on tortuosity[3] and dispersive effects; and $\boldsymbol{u}$ is a convective velocity field representing the flow of CSF in Ω_{CSF} and the flow of ISF in Ω_{PAR}. ξ models a transfer or exchange parameter between the 3D domain (Ω_{PAR} or Ω_{CSF}) and the perivascular networks Λ_a, Λ_v. To summarize,

$$\phi = \begin{cases} 1 & \text{in } \Omega_{\mathrm{CSF}} \\ \phi_{\mathrm{PAR}} & \text{in } \Omega_{\mathrm{PAR}} \end{cases}, \; D = \begin{cases} D_{\mathrm{CSF}} & \text{in } \Omega_{\mathrm{CSF}} \\ D_{\mathrm{PAR}} & \text{in } \Omega_{\mathrm{PAR}} \end{cases}, \quad \boldsymbol{u} = \begin{cases} \boldsymbol{u}_{\mathrm{CSF}} & \text{in } \Omega_{\mathrm{CSF}} \\ \boldsymbol{u}_{\mathrm{PAR}} & \text{in } \Omega_{\mathrm{PAR}} \end{cases}, \; \xi = \begin{cases} \xi_{\mathrm{CSF}} & \text{if } |\Omega^i \cap \Omega_{\mathrm{CSF}}| \neq 0 \\ \xi_{\mathrm{EF}} & \text{if } |\Omega^i \cap \Omega_{\mathrm{PAR}}| \neq 0 \end{cases}.$$

In the above, ξ is defined segment-wise: for each centerline Λ^i with surrounding PVS Ω^i, $|\Omega^i \cap \Omega_{\mathrm{PAR}}|$ (resp. $|\Omega^i \cap \Omega_{\mathrm{CSF}}|$) is nonzero whenever Ω^i intersects Ω_{PAR} (resp. Ω_{CSF}). If the surrounding PVS intersects both, then we set $\xi = \xi_{\mathrm{EF}}$ if Ω^i mainly (80 percent) intersects Ω_{PAR}, in which case the interaction with Ω_{CSF} is ignored; otherwise, we set $\xi = \xi_{\mathrm{CSF}}$.

Also in (1), the notation $\overline{c}$ denotes a lateral average of the concentration over the outer perivascular surfaces, defined for each centerline Λ^i and each point $s \in \Lambda^i$ by

$$\overline{c}(s) = \frac{1}{P(s)} \int_{\partial\Theta_2^i(s)} c$$

where $\partial\Theta_2^i(s)$ is the outer boundary of the cross-section $\Theta(s)$ of the PVS Ω^i at s and $P(s)$ is the perimeter of $\Theta(s)$. Moreover, for both the periarterial and perivenous networks (Λ_a, Λ_v with outer PVS boundaries Γ_a, Γ_v), the term δ_Γ is concentrated on the outer lateral surfaces of the PVSs, and defined in terms of its action on any sufficiently smooth function $v : \Omega \to \mathbb{R}$ such that

$$\langle \xi(\overline{c} - \hat{c})\delta_\Gamma, v \rangle = \int_\Lambda P\xi(\overline{c} - \hat{c})\overline{v},$$

under the assumption that ξ is constant on each $\partial\Theta_2^i$.

On the interface between the brain and the CSF spaces $\Gamma_{\mathrm{pia}} \cup \Gamma_{\mathrm{LV}}$, we prescribe the following interface conditions, which represent a semi–permeable interface, writing $c|_{\Omega_{\mathrm{PAR}}} = c_{\mathrm{PAR}}$ and $c|_{\Omega_{\mathrm{CSF}}} = c_{\mathrm{CSF}}$:

$$(-D\nabla(\phi c) + \boldsymbol{u}c)|_{\Omega_{\mathrm{PAR}}} \cdot \boldsymbol{n} = -(-D\nabla(\phi c) + \boldsymbol{u}c)|_{\Omega_{\mathrm{CSF}}} \cdot \boldsymbol{n} \quad \text{on} \quad \Gamma_{\mathrm{pia}} \cup \Gamma_{\mathrm{LV}}, \tag{2a}$$

$$(-D\nabla(\phi c) + \boldsymbol{u}c)|_{\Omega_{\mathrm{PAR}}} \cdot \boldsymbol{n} = \beta_{\mathrm{pia}}(c_{\mathrm{PAR}} - c_{\mathrm{CSF}}) \quad \text{on} \quad \Gamma_{\mathrm{pia}} \cup \Gamma_{\mathrm{LV}}, \tag{2b}$$

where $\boldsymbol{n} = \boldsymbol{n}_{\mathrm{PAR}}$ is the normal vector field defined over the interface, outward-pointing when viewed from Ω_{PAR}, and $\beta_{\mathrm{pia}} \geqslant 0$ is a permeability constant.

We supplement (1) and (2) with the following boundary conditions representing a given molecular influx at Γ_{SSAS}, molecular efflux at a constant update rate β_{exit} at $\Gamma_{\mathrm{AM-U}}$, and no influx or efflux elsewhere from the CSF spaces.

$$(D\nabla(\phi c) - \boldsymbol{u}c) \cdot \boldsymbol{n} = g_{\mathrm{influx}} \quad \text{on} \quad \Gamma_{\mathrm{SSAS}}, \tag{3a}$$

$$(-D\nabla(\phi c) + \boldsymbol{u}c) \cdot \boldsymbol{n} = \beta_{\mathrm{exit}} c \quad \text{on} \quad \Gamma_{\mathrm{AM-U}}, \tag{3b}$$

$$(-D\nabla(\phi c) + \boldsymbol{u}c) \cdot \boldsymbol{n} = 0 \quad \text{on} \quad \Gamma_{\mathrm{AM-L}} \cup \Gamma_{\mathrm{SC}}. \tag{3c}$$

where again $\boldsymbol{n}$ denotes the outward-pointing boundary normal.

The concentration $\hat{c} = \hat{c}(s,t)$ in the periarterial and perivenous networks ($s \in \Lambda_a, s \in \Lambda_v$), entering in (1), represents the concentration in the perivascular space averaged over each perivascular cross-section and is governed by

$$\partial_t(A\hat{c}) - \partial_s(\hat{D}A\partial_s\hat{c}) + \partial_s(A\hat{u}\hat{c}) + \xi P(\hat{c} - \overline{c}) = 0 \qquad \text{in} \quad \Lambda_a, \Lambda_v, \tag{4}$$

where in Λ_a, Λ_v refers to in each Λ^i in each of these networks. In (4), $A = A(s)$ is defined as the PVS cross-sectional area; i.e., for each $s \in \Lambda^i$ with associated PVS Ω^i, the area of the cross-section $\Theta^i(s)$. Also, $\hat{D}$ is the effective diffusion coefficient, and $\hat{u}$ is a convective velocity representing an (average) CSF flow velocity in the axial direction of the perivascular spaces.

To complete (4), we prescribe bifurcation conditions at internal nodes of the perivascular networks Λ_a, Λ_v and boundary conditions at the end nodes. To this end, define the set of internal nodes $\mathcal{B} \subset \mathcal{V}$ as the set of nodes that are connected to two or more edges and the set of end nodes as $\mathcal{N} \subset \mathcal{V}$, write $\hat{c}^i = \hat{c}|_{\Lambda^i}$, and for $y \in \mathcal{B}$ let $\mathcal{E}(y)$ denote the set of (two or three) edges in $\{\Lambda^i\}$ sharing the node y. To impose continuity of the concentrations, we set that the concentrations when viewed from each edge must match at nodes:

$$\hat{c}^i(y) = \hat{c}^j(y) \qquad \forall \Lambda^i, \Lambda^j \in \mathcal{E}(y) \qquad \forall y \in \mathcal{B}. \tag{5}$$

Moreover, to ensure mass conservation, we set that the flux going in and out at nodes should add to zero, or more precisely, that for each $y \in \mathcal{B}$:

$$\sum_{\Lambda^i \in \mathcal{E}(y)} \left(\hat{D}^i A^i \partial_s \hat{c}^i(y) - A^i \hat{u}^i(y)\hat{c}^i(y)\right) n^i(y) = 0. \tag{6}$$

Here the (normal "vector") function n^i takes the values in $\{-1, 1\}$ and defines an orientation of vertices of edge Λ^i. Specifically, for an edge Λ^i oriented from y_{in} to y_{out} we set

$$n^i(y_{\text{in}}) = 1, \quad n^i(y_{\text{out}}) = -1. \tag{7}$$

Finally, we impose a homogeneous Neumann condition at all network end nodes to augment (4):

$$\hat{D} A \partial_s(\phi \hat{c}) - A \hat{u} \hat{c} = 0 \quad \text{on} \quad \mathcal{N}. \tag{8}$$

This no-flux condition states that the network end nodes represent barriers for molecular efflux into or out of the perivascular network, and thus that all solute exchange between the PVSs and their surroundings takes place via the lateral outer PVS surface and is regulated by the exchange parameter ξ cf. (1) and (4). Larger particles have been observed to accumulate within the PVS as the surface arteries penetrate into the brain parenchyma[4,5], and (8) is appropriate to represent such behavior. However, to represent a continuously extending PVSs also along penetrating vessels, this condition should be revisited.

S1.1.3 Modelling CSF flow via the incompressible Stokes equations

The time-independent, incompressible Stokes equations model the flow of an incompressible Newtonian fluid at low Reynolds numbers, and read as follows: over the domain $\Omega_{\text{CSF}} \subset \mathbb{R}^3$, find the velocity vector field $\boldsymbol{u} : \Omega_{\text{CSF}} \to \mathbb{R}^3$ and the pressure field $p : \Omega_{\text{CSF}} \to \mathbb{R}$ such that

$$-\mu \Delta \boldsymbol{u} + \nabla p = 0 \quad \text{in } \Omega_{\text{CSF}}, \tag{9a}$$
$$\nabla \cdot \boldsymbol{u} = 0 \quad \text{in } \Omega_{\text{CSF}}. \tag{9b}$$

In addition, we impose the following boundary conditions to model flow induced by CSF production in the choroid plexus with $\Gamma_{\text{AM-U}}$ as the main efflux site:

$$(\mu \nabla \boldsymbol{u} \cdot \boldsymbol{n} - p\boldsymbol{n}) \cdot \boldsymbol{n} = -R_0(\boldsymbol{u} \cdot \boldsymbol{n}), \quad \boldsymbol{u} \cdot \boldsymbol{t} = 0 \quad \text{on } \Gamma_{\text{AM-U}}, \tag{10a}$$
$$\boldsymbol{u} = 0 \quad \text{on } \Gamma_{\text{AM-L}} \cup \Gamma_{\text{pia}} \cup \Gamma_{\text{SSAS}}, \tag{10b}$$
$$\boldsymbol{u} \cdot \boldsymbol{n} = \frac{1}{|\Gamma_{\text{LV}}|} u_{\text{in}}, \quad \boldsymbol{u} \cdot \boldsymbol{t} = 0 \quad \text{on } \Gamma_{\text{LV}}, \tag{10c}$$

where $\boldsymbol{n}$ and $\boldsymbol{t}$ denote the unit outward normal and tangent vectors to the boundary respectively, μ is the (dynamic) CSF viscosity, $R_0 > 0$ is a resistance parameter for CSF efflux, and u_{in} is a given fluid influx, here across the lateral ventricle wall Γ_{LV}. We consider alternative variations of these boundary conditions in connection with estimating dispersion effects induced by CSF pulsatility, see Section S1.3.

S1.1.4 Steady flow in perivascular networks induced by pressure differences

To model steady flow induced by pressure differences between end nodes in a perivascular network Λ, with edges $\{\Lambda^i\}_i$, internal nodes $\mathcal{B}$ and end nodes $\mathcal{N}$, we consider the following system of hydraulic network equations[6–8]. The unknowns are the PVS flux $\hat{q} : \Lambda \to \mathbb{R}$ and pressure $\hat{p} : \Lambda \to \mathbb{R}$, which represent the fluid flux and the average pressure across cross-sections of the PVSs, respectively. These are defined for each Λ^i by solving:

$$\hat{q} + \frac{A\kappa}{\mu} \partial_s \hat{p} = 0 \quad \text{in } \Lambda^i, \tag{11a}$$
$$-\partial_s \hat{q} = 0 \quad \text{in } \Lambda^i, \tag{11b}$$

where A is the area of the PVS cross-sections, μ is the CSF viscosity as before, and κ is derived from an assumption of Poiseuille flow in the annular cross-section of the PVS as[6]:

$$\kappa = \frac{1}{8}\left(R_2^2 + R_1^2 - \frac{1}{\ln(R_2/R_1)}(R_2^2 - R_1^2)\right). \tag{12}$$

The PVS flux $\hat{q}$ and the associated average PVS velocity in the axial direction $\hat{u}$ are directly related by the cross-sectional area

$$\hat{q}^i = A^i \hat{u}^i \qquad \forall \Lambda^i. \tag{13}$$

In addition, to complete (11), we impose continuity of the fluid pressure and conservation of flux at each internal node. Write $\hat{p}^i = \hat{p}|_{\Lambda^i}$. These conditions then read as: for each $y \in \mathcal{B}$ with connected edges $\mathcal{E}(y)$:

$$\hat{p}^i(y) = \hat{p}^j(y) \qquad \forall \Lambda^i, \Lambda^j \in \mathcal{E}(y), \tag{14a}$$

$$\sum_{\Lambda^i \in \mathcal{E}(y)} \hat{q}^i n^i(y) = 0. \tag{14b}$$

where n^i is as defined by (7). Finally, to drive this flow, we impose given fluid pressures p_0 at the network end nodes:

$$\hat{p}(y) = p_0(y) \qquad y \in \mathcal{N}. \tag{15}$$

In the case where modelling flow in the perivascular networks Λ_a, Λ_v induced by CSF production, we impose the fluid pressure p_{CSF} computed in the CSF spaces Ω_{CSF} (and its harmonic extensions into Ω_{PAR}) as the given fluid pressures p_0. Note that we here consider steady PVS flow in a non-moving domain; the effect of domain motion is addressed in Section S1.4.

S1.2 Numerical solution of the transport and flow equations

We solve the models presented in Section S1.1 numerically using finite element methods. The following subsections provide more details, model-by-model.

S1.2.1 Computational mesh entities: definitions and common notation

We consider a mesh $\mathcal{T} = \{E\}$ of $\Omega = \Omega_{\mathrm{PAR}} \cup \Omega_{\mathrm{CSF}}$, consisting of tetrahedral mesh cells E, and conforming to the domains Ω_{PAR} and Ω_{CSF} and to the CSF-brain interface $\Gamma_{\mathrm{pia}} \cup \Gamma_{\mathrm{LV}}$. We denote the restriction of $\mathcal{T}$ to Ω_{PAR} and Ω_{CSF} by $\mathcal{T}_{\mathrm{PAR}}$ and $\mathcal{T}_{\mathrm{CSF}}$, respectively. The collection of all interior facets (i.e. triangular faces of the tetrahedral mesh cells) in $\mathcal{T}_{\mathrm{PAR}}$ and $\mathcal{T}_{\mathrm{CSF}}$ are denoted by $\mathcal{F}_{i,\mathrm{PAR}}$ and $\mathcal{F}_{i,\mathrm{CSF}}$, respectively. We define the union of facets interior both to $\mathcal{T}_{\mathrm{PAR}}$ and $\mathcal{T}_{\mathrm{CSF}}$ as $\mathcal{F}_i = \mathcal{F}_{i,\mathrm{PAR}} \cup \mathcal{F}_{i,\mathrm{CSF}}$.

S1.2.2 Finite element solution of coupled 3D-1D solute transport equations

We consider the system of coupled 3D-1D solute transport equations given by (1) and (4) with the interface conditions (2), the bifurcation conditions (5) and (6), and the boundary conditions (3) and (8). We discretize these equations using an implicit finite difference scheme in time, a discontinuous Galerkin (DG) finite element method with upwinding in space for the 3D domain to accurately capture sharp boundary layers, and a continuous Galerkin method for the 1D networks. We remark that the transport in the CSF spaces is highly convection dominated, with an average Péclet number of 402 and maximum of 9542 (assuming a characteristic length of 10 cm, and accounting for the increased diffusivity due to dispersion).

We first consider the discretization of (1) and introduce the discrete space

$$V_h = \{c \in L^2(\Omega) : \, c|_E \in \mathrm{P}^1(E), \, E \in \mathcal{T}\}, \tag{16}$$

where $L^2(\Omega)$ is the space of square-integrable functions defined over Ω and $\mathrm{P}^1(E)$ denotes the space of polynomials of total degree $\leqslant 1$ defined over the tetrahedra E. To discretize the diffusion term in (1), we use a symmetric weighted interior penalty DG formulation, referring to[9] and [10, Section 4.5.2.3] for details on this method. Recall that ϕ is constant in each domain Ω_{PAR} and Ω_{CSF}, and thus in particular that $\nabla(\phi c) = \phi \nabla c$ on each $E \in \mathcal{T}$. Define for $c, v \in V_h^k$:

$$a_h(c,v) = \sum_{E \in \mathcal{T}} \int_E D\phi \nabla c \cdot \nabla v - \sum_{F \in \mathcal{F}_i} \int_F (\{D\phi \nabla c\}_w \cdot \boldsymbol{n}_F [v] + \{D\phi \nabla v\}_w \cdot \boldsymbol{n}_F [c]) + \sum_{F \in \mathcal{F}_i} \eta \frac{\gamma_{D,F}}{h_F} \int_F [c][v]. \tag{17}$$

In (17), for each facet $F \in \mathcal{F}^i$ shared between cells E^1 and E^2, we associate a facet normal vector $\boldsymbol{n}_F$ pointing from E^1 to E^2. The facet diameter is denoted by h_F, the jump $[\cdot]$ is given by $[v] = v|_{E^1} - v|_{E^2}$, and the unweighted average $\{\cdot\}$ and weighed average $\{\cdot\}_w$ are defined as:

$$\{v\} = \frac{1}{2} v|_{E^1} + \frac{1}{2} v|_{E^2}, \qquad \{v\}_w = \frac{\kappa_2}{\kappa_1 + \kappa_2} v|_{E^1} + \frac{\kappa_1}{\kappa_1 + \kappa_2} v|_{E^2} \quad \text{where} \quad \kappa_i = (D\phi)|_{E^i}. \tag{18}$$

The parameter $\gamma_{D,F}$ is the harmonic mean of the porosity-weighted diffusion coefficient given by

$$\gamma_{D,F} = \frac{2\kappa_1 \kappa_2}{\kappa_1 + \kappa_2}, \tag{19}$$

and η is a user-specified penalty parameter (we set $\eta = 1000$). To discretize the convection term in (1), we use upwinding, see [10, Section 2.3.1] and the references therein. For $c, v \in V_h^k$, define

$$a_h^{\mathrm{up}}(c,v) = -\sum_{E\in\mathcal{T}}\int_E c\boldsymbol{u}\cdot\nabla v + \sum_{F\in\mathcal{F}_i}\int_F \{\boldsymbol{u}c\}\cdot\boldsymbol{n}_F[v] + \sum_{F\in\mathcal{F}_i}\int_F \frac{|\boldsymbol{u}\cdot\boldsymbol{n}_F|}{2}[c][v]. \tag{20}$$

Our discrete formulation for (1) with the interface conditions (2) and boundary conditions (3) and given initial conditions c_h^0 then reads: for $n = 1, 2, \ldots$, with $t^n - t^{n-1} = \tau$, find $c_h^n \in V_h$ such that for all $v \in V_h$:

$$\int_\Omega \frac{1}{\tau}(\phi c_h^n - \phi c_h^{n-1})v + a_h(c_h^n, v) + a_h^{\mathrm{up}}(c_h^n, v) + \int_{\Gamma_{\mathrm{pia}}\cup\Gamma_{\mathrm{LV}}} \beta_{\mathrm{pia}}[c_h^n][v] + \int_{\Gamma_{\mathrm{AM-U}}} \beta_{\mathrm{exit}} c_h^n v + \int_\Lambda \xi P\left(\overline{c_h^n} - \hat{c}_h^n\right)\overline{v} = \int_{\Gamma_{\mathrm{SSAS}}} g_{\mathrm{influx}} v. \tag{21}$$

To discretize (4) with the bifurcation conditions (5) and (6), and the boundary conditions (8), we use the space of continuous piecewise linear polynomials defined over Λ:

$$\hat{V}_h = \{v \in C^0(\Lambda),\ v|_{\Lambda^i} \in \mathrm{P}^1(\Lambda^i)\}, \tag{22}$$

where $\mathrm{P}^1(\Lambda^i)$ is the space of linear polynomials on each Λ^i. The discrete formulation then reads: for $n = 1, 2, \ldots$, find $\hat{c}_h^n \in \hat{V}_h$ such that for all $\hat{v} \in \hat{V}_h^k$:

$$\int_\Lambda \frac{1}{\tau}(A\hat{c}_h^n - A\hat{c}_h^{n-1})\hat{v} + \int_\Lambda \hat{D}A\partial_s\hat{c}_h^n\partial_s\hat{v}^n - \int_\Lambda A\hat{u}\hat{c}_h^n\partial_s\hat{v} + \int_\Lambda \xi P(\hat{c}_h^n - \overline{c_h^n})\hat{v} + a_h^{\mathrm{stab}}(\hat{u};\hat{c},\hat{v}) = 0. \tag{23}$$

In the above, if $\hat{u}$ is non–zero on Λ^i, then the artificial diffusion a_h^{stab} stabilization term is nonzero and is given below, for more details see for [11, Section 12.6].

$$a_h^{\mathrm{stab}}(\hat{u};\hat{c},\hat{v}) = \frac{1}{\|\hat{u}\|_{L^2(\Lambda^i)}} h_{\Lambda^i} \int_{\Lambda^i} A(\hat{u}\partial_s\hat{c}_h)(\hat{u}\partial_s\hat{v}), \tag{24}$$

where h_{Λ^i} is the mesh–size of Λ^i. Note that the condition (6) is enforced weakly in the above formulation.

Summary. The discretization for (1) and (4) complemented with boundary conditions ((3) and (8)), interface and bifurcation conditions ((2), (14), and (5)), and intial conditions $c_h^0 = 0$ and $\hat{c}_h^0 = 0$ is the following:

For $n = 1, 2, \ldots$, find $c_h^n \in V_h$ and $\hat{c}_h^n \in \hat{V}_h$ such that the coupled equations (21) and (23) hold for all $v \in V_h$ and for all $\hat{v} \in \hat{V}_h$.

S1.2.3 Finite element solution of the incompressible Stokes equations

We consider an H(div)-based finite element approximation of the incompressible Stokes equations (9) defined over Ω_{CSF} with the boundary conditions (10). Following[12], we approximate the velocity field $\boldsymbol{u}$ and the pressure field p with the following finite element spaces:

$$\boldsymbol{V}_{h,g} = \{\boldsymbol{v} \in H(\mathrm{div},\Omega_{\mathrm{CSF}}) :\ \boldsymbol{v}|_E \in \mathrm{BDM}^2(E),\ E \in \mathcal{T}_{\mathrm{CSF}};\ \boldsymbol{v}\cdot\boldsymbol{n} = 0 \text{ on } \Gamma_{\mathrm{pia}}\cup\Gamma_{\mathrm{AM-L}}\cup\Gamma_{\mathrm{SSAS}},\ \ \boldsymbol{v}\cdot\boldsymbol{n} = g \text{ on } \Gamma_{\mathrm{LV}}\}$$
$$Q_h = \{q \in L^2(\Omega_{\mathrm{CSF}}) :\ q|_E \in \mathrm{P}^1(E),\ E \in \mathcal{T}_{\mathrm{CSF}}\}.$$

Here, $H(\mathrm{div},\Omega_{\mathrm{CSF}})$ is the space of $L^2(\Omega_{\mathrm{CSF}})$ vector fields with $L^2(\Omega_{\mathrm{CSF}})$ divergence, BDM^2 is the Brezzi-Douglas–Marini element[13] of degree 2, g is a given constant, and $\boldsymbol{n}$ is the unit outward normal vector to each facet. Given any vector $\boldsymbol{v}$, the normal and tangential components on each facet are denoted and given by

$$\boldsymbol{v}_n = (\boldsymbol{v}\cdot\boldsymbol{n})\boldsymbol{n}, \quad \boldsymbol{v}_t = \boldsymbol{v} - \boldsymbol{v}_n.$$

Since $\boldsymbol{V}_{h,g} \subset H(\mathrm{div},\Omega_{\mathrm{CSF}})$, then $[\boldsymbol{v}_n] = 0$ on $\mathcal{F}_{i,\mathrm{CSF}}$, the interior facets to Ω_{CSF}. Continuity in the tangential component is enforced weakly via interior penalization. For convenience, we collect all facets exterior to the CSF space $\Gamma_{\mathrm{AM-U}}$ in the set

$$\mathcal{F}_e = \mathcal{F}_{\mathrm{pia}}\cup\mathcal{F}_{\mathrm{LV}}\cup\mathcal{F}_{\mathrm{AM-L}}\cup\mathcal{F}_{\mathrm{AM-U}}\cup\mathcal{F}_{\mathrm{SSAS}},$$

where facets lying on the pial interface Γ_{pia} are denoted by $\mathcal{F}_{\mathrm{pia}}$, on the lower and upper outer (arachnoid) boundary $\Gamma_{\mathrm{AM-L}}$ and $\Gamma_{\mathrm{AM-U}}$ by $\mathcal{F}_{\mathrm{AM-L}}$ and $\mathcal{F}_{\mathrm{AM-U}}$, respectively, on the boundary towards the spinal SAS Γ_{SSAS} by $\mathcal{F}_{\mathrm{SSAS}}$, and on the surface of the lateral ventricles by $\mathcal{F}_{\mathrm{LV}}$. Now, define the form

$$\mathcal{A}_h(\boldsymbol{u},\boldsymbol{v}) = \sum_{E\in\mathcal{T}_{\mathrm{CSF}}}\int_E \mu\nabla\boldsymbol{u} : \nabla\boldsymbol{v} + \sum_{F\in\mathcal{F}_{i,\mathrm{CSF}}\cup\mathcal{F}_e}\left(-\int_F \mu\{\nabla\boldsymbol{u}\}\boldsymbol{n}_F\cdot[\boldsymbol{v}_t] - \int_F \mu\{\nabla\boldsymbol{v}\}\boldsymbol{n}_F\cdot[\boldsymbol{u}_t] + \int_F \frac{\sigma\mu}{h_F}[\boldsymbol{u}_t]\cdot[\boldsymbol{v}_t]\right), \tag{25}$$

where on exterior facets the average and jump operators take the one-sided values. We set the penalty parameter for the tangential continuity to be $\sigma = 20$. The finite element discretization of the incompressible Stokes equations is then to find $(\boldsymbol{u}_h, p_h) \in \boldsymbol{V}_{h,g} \times Q_h$ with $g = \frac{1}{|\Gamma_{\mathrm{LV}}|} u_{\mathrm{in}}$ such that

$$\mathcal{A}_h(\boldsymbol{u}_h, \boldsymbol{v}_h) + \sum_{F \in \mathcal{F}_{\mathrm{AM-U}}} \int_F R_0 (\boldsymbol{u}_h \cdot \boldsymbol{n})(\boldsymbol{v}_h \cdot \boldsymbol{n}) - \int_{\Omega_{\mathrm{CSF}}} \nabla \cdot \boldsymbol{v}_h \, p_h = 0 \qquad \forall \boldsymbol{v}_h \in \boldsymbol{V}_{h,0} \tag{26a}$$

$$\int_{\Omega_{\mathrm{CSF}}} \nabla \cdot \boldsymbol{u}_h \, q_h = 0 \qquad \forall q_h \in Q_h. \tag{26b}$$

S1.2.4 Finite element solution of the perivascular network equations

We consider meshes $\mathcal{I}_a, \mathcal{I}_v$ representing a conforming subdivision of each of the perivascular networks Λ_a, Λ_v. Relative to each mesh $\mathcal{I}$, we define the space of (discontinuous) piecewise constants $\hat{Z}_h(\mathcal{I})$ and define spaces of continuous piecewise linears $\hat{V}_{h,g}(\mathcal{I})$ with prescribed boundary node values (on $\mathcal{N}$) given by g:

$$\hat{Z}_h(\mathcal{I}) = \{z \in L^2(\Lambda); z|_{\Lambda_i} \in \mathrm{P}^0(\Lambda_i) \forall \Lambda^i \in \mathcal{I}\}, \tag{27}$$

$$\hat{V}_{h,g}(\mathcal{I}) = \{v \in C^0(\Lambda); v|_{\Lambda^i} \in \mathrm{P}^1(\Lambda_i), v(x) = g(x) \forall x \in \mathcal{N}\}. \tag{28}$$

To discretize (11) with the bifurcation conditions (14) and boundary conditions (15), we use the space of continuous functions $\hat{Z}_h(\mathcal{I})$ to enforce the continuity of the pressure at bifurcation points, while the conservation of flux is enforced (weakly) through the variational formulation. The discrete variational form of the equations then reads: Find $(\hat{q}, \hat{p}) \in \hat{Z}_h(\mathcal{I}) \times \hat{V}_{h,p_0}(\mathcal{I})$ such that

$$\langle \hat{q}, z \rangle + \langle z, \frac{A\kappa}{\mu} \partial_s \hat{p} \rangle = 0 \quad \forall z \in \hat{Z}_h(\mathcal{I}) \tag{29a}$$

$$\langle \hat{q}, \partial_s w \rangle = 0 \quad \forall w \in \hat{V}_{h,0}(\mathcal{I}). \tag{29b}$$

where $\langle \cdot, \cdot \rangle$ denotes the $L^2(\mathcal{I})$-inner product and defined segment-wise. For a stability and convergence analysis of this discrete model, we refer to the reference[8].

S1.3 Estimating dispersion factors from pulsatile CSF flow

The cardiac (~1Hz) and respiratory (~0.25Hz) cycles induce pulsatile flow of CSF in the ventricular system and in the cranial and spinal SAS. Pulsatile flow leads to dispersion which in turn may enhance molecular transport[14–19]. To account for the dispersive effects over a longer time scale (hours to days), and in the absence of measurements or estimates of dispersion coefficients in human CSF spaces, we adapt existing theoretical estimates[15,17]. More specifically, we compute spatially-varying dispersion enhancement fields R_c and R_r (Fig. 2G, I), associated with the cardiac and respiratory cycles respectively, via the algorithm presented below. These fields then contribute to the diffusion coefficient in Ω_{CSF} in (1) as $D = (1 + R_c + R_r) D^{\mathrm{Gad}}$.

i) To account for viscous forces, we compute spatially-varying CSF pressure fields p_c^0, p_r^0 in Ω_{CSF} corresponding to the Stokes flow induced by the peak volumetric reduction of the CSF space in the respective cycle (Fig. 2F, H). More precisely, we numerically solve the incompressible Stokes equations (9) equipped with the following boundary conditions mimicking a dilation of the brain parenchyma with the spinal SAS as the only route for CSF efflux:

$$\boldsymbol{u} = 0 \text{ on } \Gamma_{\mathrm{Pia}}; \quad \mu \nabla \boldsymbol{u} \cdot \boldsymbol{n} - p\boldsymbol{n} = 0 \text{ on } \Gamma_{\mathrm{SSAS}}; \quad \boldsymbol{u} = \frac{u_{\mathrm{LV}}^{\mathrm{in}} \cdot \boldsymbol{n}}{|\Gamma_{\mathrm{LV}}|} \text{ on } \Gamma_{\mathrm{LV}}; \quad \boldsymbol{u} = \frac{u_{\mathrm{AM}}^{\mathrm{in}} \cdot \boldsymbol{n}}{|\Gamma_{\mathrm{skull}}|} \text{ on } \Gamma_{\mathrm{AM}}. \tag{30}$$

In the cardiac cycle case, we set $u_{\mathrm{AM}}^{\mathrm{in}} = 6\,\mathrm{ml/s}$[20,21] and $u_{\mathrm{LV}}^{\mathrm{in}} = 0.31\,\mathrm{ml/s}$[22] to solve for p_c^0. In the respiratory cycle case, we set $u_{\mathrm{AM}}^{\mathrm{in}} = 1\,\mathrm{ml/s}$[23] and $u_{\mathrm{LV}}^{\mathrm{in}} = 0.121\,\mathrm{ml/s}$[24] to solve for p_r^0.

ii) We also estimate the Womersley numbers α_c, α_r associated with the cardiac and respiratory flow patterns, respectively, by the definition

$$\alpha_i^2 = \frac{h_{\mathrm{SAS}}^2 \omega_i \rho}{\mu} \qquad i \in \{c, r\}, \tag{31}$$

with CSF density $\rho = 10^3\,\mathrm{kg/m^3}$, a mean CSF space width $h_{\mathrm{SAS}} = 1.5\mathrm{mm}$, and CSF viscosity μ given in Table. 1. For the cardiac cycle, we consider an angular frequency $\omega_c = 2\pi$, while for the respiratory cycle, we set $\omega_r = 0.5\pi$. The resulting (square) Womersley numbers are $\alpha_c^2 = 20.2$ for the cardiac cycle and $\alpha_r^2 = 5.05$ for the respiratory cycle.

Parameter	Description	Value(s)	Ref.
Relative PVS size β	$\beta = \beta_i = R_2^i/R_1^i$	2	≈[27]
Wave frequency f	Traveling wave frequency of vascular motion	0.1 – 1.0 Hz	[26]
Wave length λ	Traveling wave length of vascular motion	0.02 – 2 mm	[26,28]
Wave amplitude	Relative amplitude of inner wall motion	1 – 10%	[26]
Cardiac frequency f_c	Frequency of human cardiac pulse wave	1.0 Hz	[29]
Cardiac wave length λ_c	Wave length of human cardiac pulse wave	2.0m	
Cardiac amplitude ε_c	Wall displacement amplitude of cardiac pulse wave	1%	
Vasomotion frequency f_v	Frequency of slow vasomotion wave	0.1 Hz	[29]
Vasomotion wave length λ_v	Wave length of vasomotion wave	0.02 m	[26,28]
Vasomotion amplitude ε_v	Wall displacement amplitude of vasomotion wave	10%	[26,28]

Table 1. Perivascular flow induced by vascular wall motion: overview of parameters.

iii) To account for inertial forces in addition to the viscous forces, we use the Womersley numbers α_c, α_r to calculate upscaled pressure fields p_c^1, p_r^1 from p_c^0, p_r^0 as:

$$p_i^1(x) = \left(1 + \frac{\alpha_i^2}{8}\right) p_i^0(x) \qquad \text{for } x \in \Omega_{\text{CSF}}, \qquad i \in \{c, r\}. \tag{32}$$

Note that this scaling is based on theoretical considerations on the ratio of oscillatory flow to steady flow impedances in a tube [25, Chap. 4.3.].

iv) Further, assuming unsteady dispersion, we follow Sharp et al.[17] to estimate local enhancement factors S_c, S_r from the non-dimensionalized pressure gradients:

$$S_i(x) = \frac{1}{\alpha_i^3} \frac{1}{\omega_i \mu / h_{\text{SAS}}} |\nabla p_i^1(x)| \qquad i \in \{c, r\}. \tag{33}$$

v) Finally, we define the cardiac and respiratory dispersion enhancement factors R_c and R_r by smoothing S_c and S_r, respectively, to account for the non-local nature of dispersion. Specifically, for $i \in \{c, r\}$, we define $R_i : \Omega_{\text{CSF}} \to \mathbb{R}^+$ by solving a heuristic weighted Helmholtz problem over Ω_{CSF} with S_i as the right-hand side:

$$-10^{-4} \Delta R_i + R_i = S_i \quad \text{on } \Omega_{\text{CSF}} \qquad \text{and} \qquad \nabla R_i \cdot \boldsymbol{n} = 0, \quad \text{on } \partial\Omega_{\text{CSF}}. \tag{34}$$

Considering the uncertainty associated with the validity of simplifying assumptions, the resulting estimates of the cardiac and respiratory dispersion factors R_c and R_r should be viewed as heuristic rather than absolute.

S1.4 Estimating net perivascular flow induced by peristaltic waves

We use the theoretical framework previously introduced by Gjerde et al.[26] to compute an analytic estimate of the time-averaged (or *net*) flow rates $\langle Q_i' \rangle$ (mm^3/s) induced by peristaltic pumping in a perivascular network $\Lambda = \cup_i \Lambda_i$. The motion of the (inner) vascular wall is described by a periodic traveling (peristaltic) wave of relative amplitude ε, wave length λ (mm) and frequency f, acting normal to the wall. By definition, the wave number is $k = 2\pi/\lambda$ and the angular frequency is $\omega = 2\pi f$. Each PVS segment Λ_i has length L_i with wave-relative length $\ell_i = kL_i$, baseline inner radius R_1^i, fixed outer radius R_2^i, and outer-to-inner ratio $\beta_i = R_2^i/R_1^i$. These geometric parameters and the assumption of annular cylindrical PVS segments yield hydraulic resistances $\mathcal{R}_{o,i}$ and additional characteristic parameters, see[26] for the complete definitions and schematics. Since the analytical estimate is derived under the assumption that $kL_i \approx O(1)$[26] and has been verified against numerical simulations for kL_i of the order $10^{-1} - 10^2$ [26, Table I], we consider it applicable for the wave lengths and vascular network data considered here in which kL_i range from 0.15 to 30 for the strong vasomotion and 0.0015 to 0.30 for the cardiac waves (Table 1).

This theoretical formalism[26] is defined relative to a network in the form of a directed, bifurcating tree with a single supply node/root i_0. To extend to a network of cerebral arteries with multiple supply nodes (such as the basilar and two internal carotid arteries in the current data set[30]), we separate the network Λ into edge-disjoint subnetworks $\Lambda^1, \Lambda^2, \Lambda^3$, one for each of the supply nodes (Fig. 1A–B, Figure S1). Each node is assigned to the subnetwork associated with the nearest supply node, and edges between nodes are preserved (Figure S1B). Next, we compute a minimal, bifurcating and directed tree representation

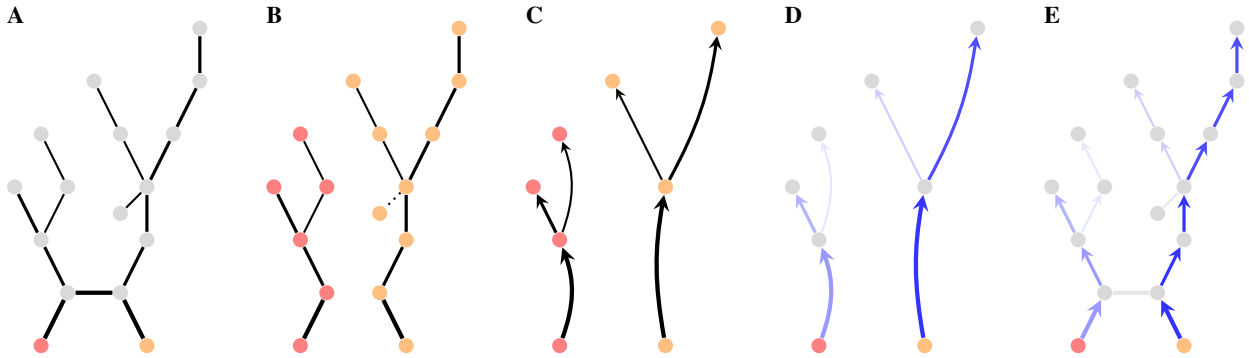

Figure S1. Estimating the perivascular flow induced by vascular wall motion. For a vascular network with vessels represented by edges of varying radii and length connected at nodes (**A**), and one or more supply nodes (here two, marked in red and orange), we compute one subnetwork for each supply node by proximity (**B**). Each subnetwork is reduced to a minimal, bifurcating and directed tree while preserving path lengths and averaging radii (**C**) which is then used to compute the net flow induced by the peristaltic wave in each branch of the minimal subnetworks (**D**). Finally, we distribute the computed flow onto the original segments (**E**).

of each subnetwork: $\mathcal{T}^1, \mathcal{T}^2, \mathcal{T}^3$ (Figure S1C). Each tree $\mathcal{T}^j = \cup E_n^j$ consists of the subset of the nodes from Λ^j that have degree 1 (are leaf or root nodes) or degree 3 (are true bifurcation points), and each path between nodes with degree $\neq 2$ in Λ^j is represented in $\mathcal{T}^j$ by an edge E^j with edge length L corresponding to the total length of the original path and edge radius R^j as the average of the path radii.

For each subtree $\mathcal{T}^j = \cup_n E_n^j$, we compute the time-averaged downstream flow rate $\langle Q_n' \rangle$ induced by the vascular wall motion for each edge n via [26, eq. (5), (34)] (Figure S1D). We next assign this flow rate $\langle Q_n' \rangle$ to each of the branches Λ_i that form the path E_n^j, thus yielding $\langle Q_i' \rangle$ for each perivascular segment Λ_i while ensuring that mass is conserved (Figure S1E). For the segment(s) ignored in the separation step (Figure S1B), we set a flow rate of zero. Finally, we define the mean longitudinal perivascular velocity induced by the peristaltic wave $\langle \hat{u}_i^x \rangle$ by dividing the flow rate $\langle Q_i' \rangle$ by the cross-section area $A_i = \pi({R_2^i}^2 - {R_1^i}^2) = \pi(\beta_i^2 - 1){R_1^i}^2$.

S1.5 Numerical verification

We assess the numerical accuracy and convergence of our simulation results by performing a series of experiments with different spatial and temporal resolutions. Specifically, we generate a sequence of three meshes (Figure S2) with an increasing number of computational mesh vertices and cells, solve all relevant simulation steps (CSF flow and intracranial transport computations) for the baseline model on each mesh, and compare the results across meshes with respect to a set of key quantities of interest. The mesh refinement employed here is localized near expected sharp concentration gradients. This allows us to better capture dynamics and reduce undershoots, see Figure S3. Similarly, we investigate the effect of the time step size by solving the intracranial transport model on the standard resolution mesh with different time steps: 1, 2, and 4 minutes.

Considering the mean tracer concentrations in the CSF, parenchyma and arterial and venous PVS domain over the first 24 h after injection, we observe negligible changes with both mesh and time refinement (Figure S3 and Figure S5). As an additional verification step, we compute the mean and maximum dispersion enhancement factor, the maximum CSF pressure and velocity in both the cardiac-driven and CSF production-induced flow fields, and mean concentrations at 3, 6, 12 and 24 h for all mesh resolutions and time steps (Figure S4). While the maximum dispersion factor increases by about 60 % from the low resolution to the standard mesh, it stabilizes with the next refinement step. All other quantities change with less than 10 % with mesh refinement, and less than 1 % with time refinement. We thus conclude that the standard resolution mesh and a time step of 2 min offer sufficient accuracy for our simulations, and remark that all reported results are obtained with the standard resolution mesh.

Finally, to check for numerical mass conservation, we perform an additional simulation not allowing for tracer efflux across the outer boundary, and confirm that the total amount of tracer is preserved over time after the initial influx phase (Figure S6).

S2 Supplementary discussion

S2.1 Extended model validation

In addition to the comparison of our in-silico predictions of tracer enrichment and clearance against glymphatic MRI, we here compare auxiliary model quantities against the literature as additional model validation.

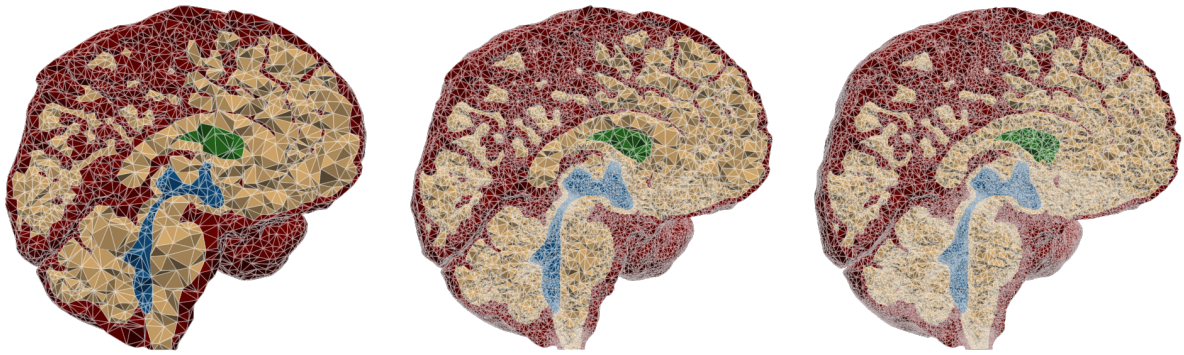

Figure S2. Illustration of the three different meshes; from left to right: low resolution, standard resolution, high resolution.

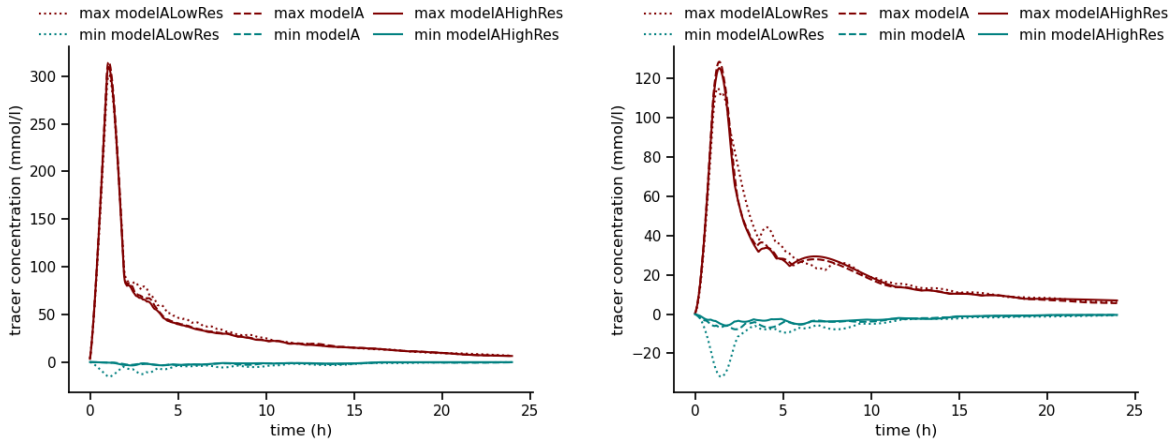

(a) Minimum and maximum tracer concentration in the CSF under mesh refinement

(b) Minimum and maximum tracer concentration in the parenchyma under mesh refinement

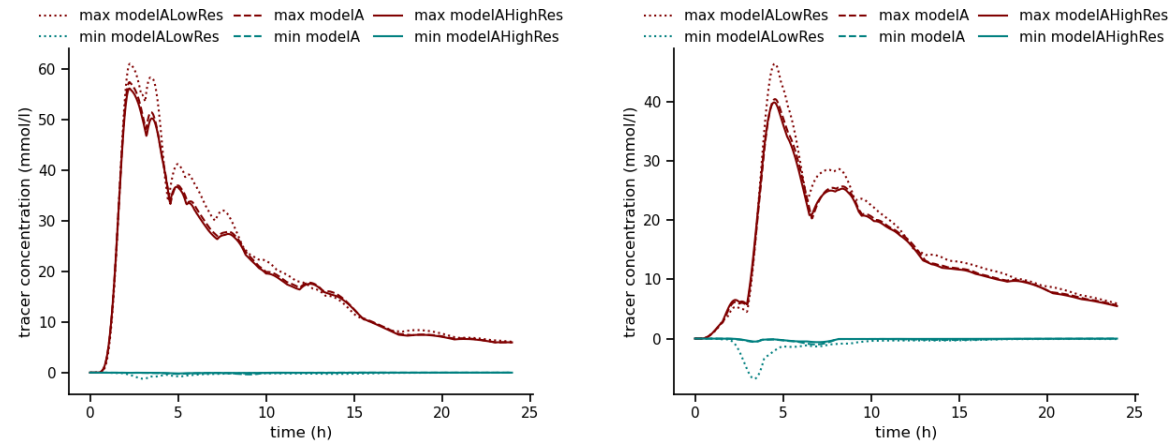

(c) Minimum and maximum tracer concentration in PVSs around arteries under mesh refinement

(d) Minimum and maximum tracer concentration in PVSs around veins under mesh refinement

Figure S3. Minimum and maximum tracer concentrations over the first 24 h after injection on the CSF and parenchyma (a), and the arterial and venous PVS (b) computed on the low resolution (LowRes), standard and high resolution (HighRes) meshes with a timestep of 2 min for the baseline model (Model A).

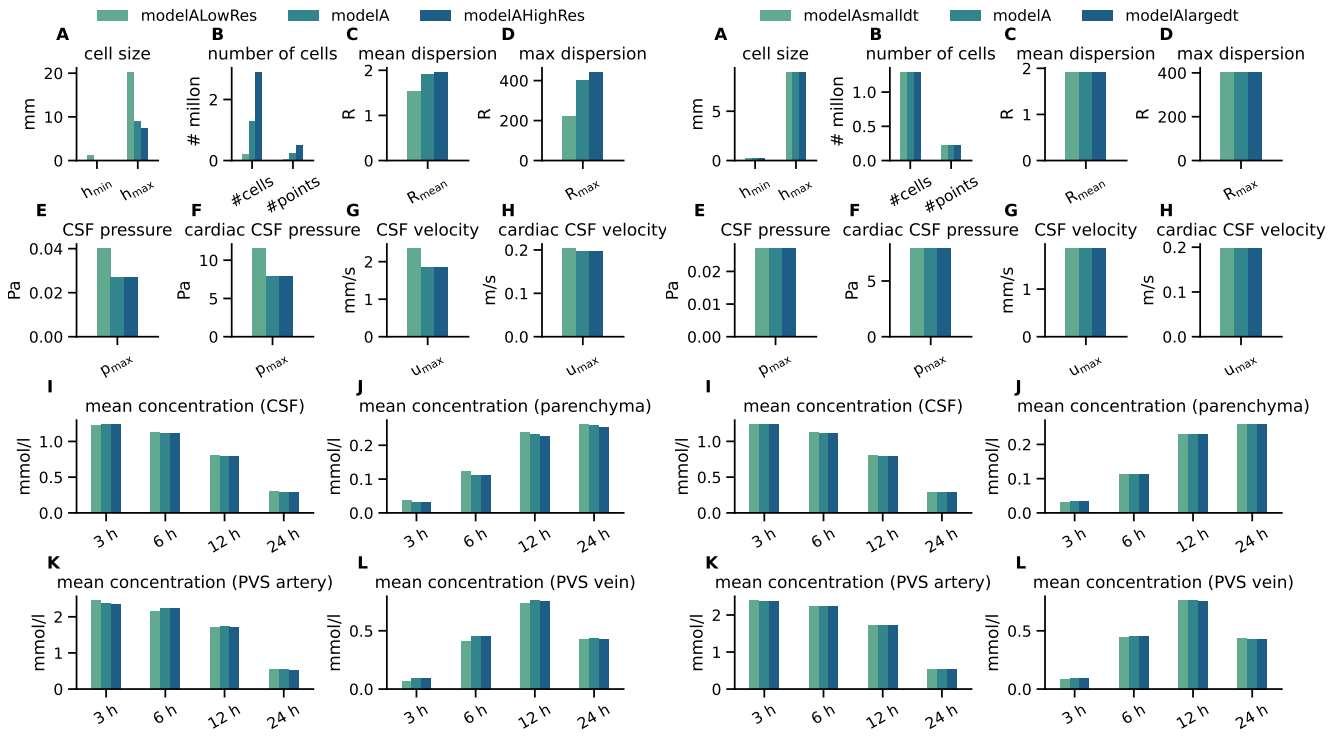

Convergence of key quantities of interest with mesh refinement

Convergence of key quantities of interest with time refinement

Figure S4. For both left and right panels: A: Minimal (h_{min}) and maximal (h_{max}) mesh cell sizes (computed as cell circumradius ×2); B: number of mesh vertices and tetrahedral cells in each mesh; C: mean cardiac dispersion enhancement factor R; D: maximum cardiac dispersion enhancement factor R; E: maximum pressure in steady CSF production flow; F: maximum pressure in cardiac-driven CSF flow; G: maximum CSF velocity in steady CSF production flow; H: maximum CSF velocity in cardiac-driven CSF flow; I–L: mean tracer concentration in the CSF, parenchyma, arterial PVS and venous PVS after 3, 6, 12 and 24 hours.

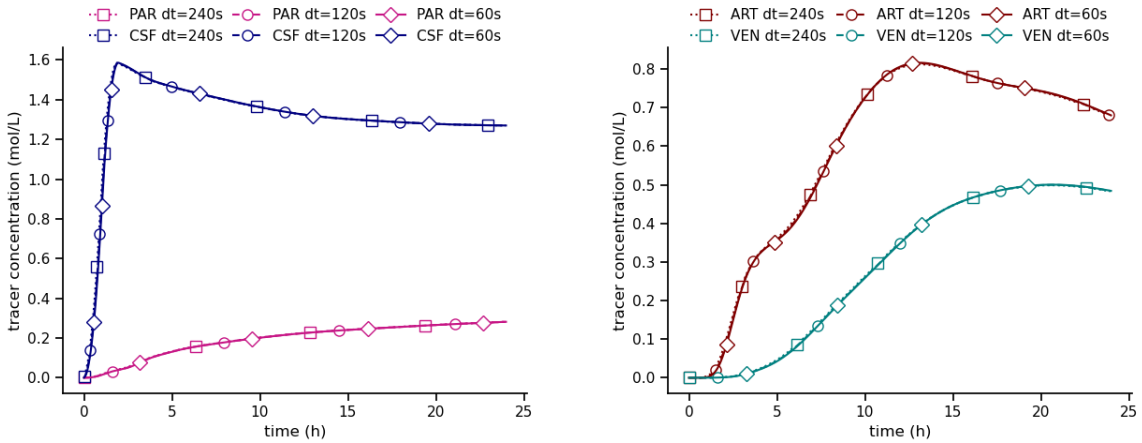

(a) Mean tracer concentration in CSF and parenchyma under time step refinement

(b) Mean tracer concentration in PVSs around (veins and) arteries under time step refinement

Figure S5. Mean tracer concentrations after up to 24 h in the CSF and parenchyma (a), and the arterial and venous PVS (b) computed on the standard resolution mesh for timesteps of 1, 2, and 4 minutes (dt of 60, 120, or 240 seconds)

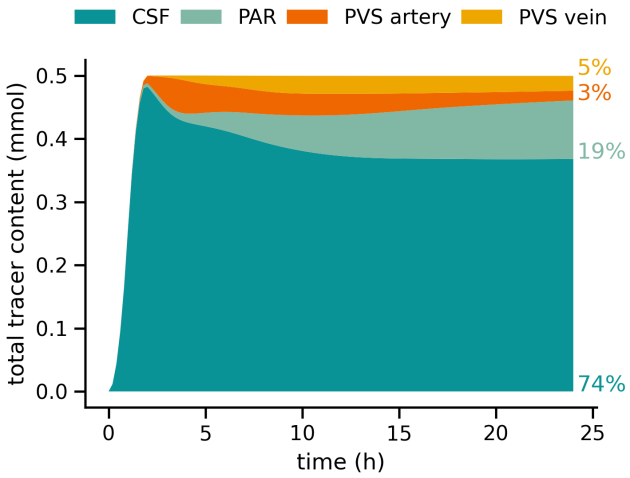

Figure S6. Total tracer content in the CSF, parenchyma, and arterial and venous PVS for a variant of the baseline model without tracer outflow. The total amount of tracer is constant after the initial influx phase demonstrating that the numerical scheme conserves mass globally.

CSF flow and pressures in the SAS and ventricular system The dynamics of human CSF flow and pressure are better quantified, by way of clinical imaging, in-vitro studies, and computational modelling, in other areas of the ventricular system[20,22,31–35]. Linninger et al[31] model CSF flow and pressure dynamics induced by CSF production and cardiac pulsatility under normal and hydrocephalic conditions, and report of very good agreement with Cine (phase-contrast) MRI measurements. Our estimates of the maximum intracranial pressure difference, 10 Pa from the cardiac contribution and 26 mPa from CSF production, is in perfect agreement with their maximum transmantle pressure difference of ~10 Pa, and also in very good agreement with mean pressure differences of 11.5 Pa measured clinically between sensors placed subdurally and in the lateral ventricle[22]. Liu et al[35] report of cardiac and respiratory pressure differences across the aqueduct of 12.1 ± 5.7 Pa and 9.5 ± 7.2 Pa, respectively; thus our baseline estimate of the respiratory contribution 1.4 Pa may be an underestimation. On the other hand, our cardiac- and respiratory-driven CSF flow estimates peak at 19.8 cm/s and 4.8 cm/s in the caudal direction, respectively, which are higher than phase-contrast MRI measurements of cardiac and respiratory CSF flow components[36,37]. Some variation in CSF flow velocities is expected considering that the values from MRI represent averages[37] and that the geometry of the CSF spaces strongly affects peak velocities[20,22]. Hornkjøl et al[33] model the flow dynamics induced by CSF production in the choroid plexus and report a peak CSF velocity of 8.9 mm/s in the aqueduct, which is 4.8 × higher than our values of 1.85 mm/s. Given that we use the same production rate, this deviation again illustrates the impact of potential differences in the (aqueduct) geometry on local velocities.

Dispersion in the SAS, ventricular system and PVS This pulsatile flow of CSF in the SAS, ventricular system and PVSs leads to an increase in effective solute diffusivity[16–18,38,39] via a process known as Taylor dispersion[14,15]. Previous estimates of the magnitude of this effect in the CSF spaces vary significantly: from an enhancement factor of 0.05–1 in periarterial spaces surrounding penetrating arteries[16,19], to 5–100 in the spinal subarachnoid space[17,38,39], and up to more than 10 000 in surface periarterial spaces[17,18]. The large variability can (at least partly) be attributed to methodological differences; e.g. different assumptions on the medium, domain width, pressure differences and/or fluid velocities, the diversity of CSF flow characteristics, as well as a high likelihood of spatial variations. Hornkjøl et al[33] consider model variations with constant dispersion factors from 1 up to 1000, and indicate that a value of 10 gives the better agreement with the clinically observed enrichment. Our spatially-varying estimates of the dispersion enhancement factors R_c, R_r (with $D = (1 + R_c + R_r)D^{\mathrm{Gad}}$) range from 0 to 200 for the cardiac contribution R_c and 0 to 320 for the respiratory contribution R_r; and is thus compatible within the previously reported spectrum.

Shapes, sizes and structures of the PVS The shapes, sizes and structures of the PVSs likely vary between species (e.g. mice vs. humans), between spatial compartments (e.g. surface vs. parenchymal), between vessel types (arteries vs. arterioles vs. veins), and in pathologies[4,5,27,40–46]. In terms of shape, the PVSs are commonly represented as annular (elliptic) cylinders, though it is well recognized that this represents an idealization[4,44–48]. In terms of sizes, Raicevic et al[45] note that the variation in PVS area is larger between PVS segments than along a single PVS segment and that the PVS area increases with lumen area. In

mice, reports of the ratio between PVS and lumen area range from ≈0.35–0.43[44] up to ≈1.12–1.4[4,45]. In humans, the PVS may be as wide as the associated surface artery and up to 4× wider in iNPH subjects[27], which would correspond to substantially larger PVS area ratios (3 or higher). To reflect the human scale, we here represent each PVS segment as an annular cylinder with inner radius R_1 and outer radius R_2 of width and area proportional to that of the corresponding blood vessel ($R_2 = 2R_1$ at baseline, $R_2 = 3R_1$ for enlarged PVS). The hydraulic resistance of annular cross-sections is $1-6\times$[47] larger than more elongated cross-sections and thus our estimates of the pressure-induced PVS velocities are conservative.

References

1. Masri, R., Zeinhofer, M., Kuchta, M. & Rognes, M. E. The modelling error in multi-dimensional time-dependent solute transport models. *ESAIM: Math. Model. Numer. Analysis* **58**, 1681–1724 (2024).
2. Laurino, F. & Zunino, P. Derivation and analysis of coupled PDEs on manifolds with high dimensionality gap arising from topological model reduction. *ESAIM: Math. Model. Numer. Analysis* **53**, 2047–2080 (2019).
3. Syková, E. & Nicholson, C. Diffusion in brain extracellular space. *Physiol. reviews* **88**, 1277–1340 (2008).
4. Mestre, H. *et al.* Flow of cerebrospinal fluid is driven by arterial pulsations and is reduced in hypertension. *Nat. communications* **9**, 4878 (2018).
5. Bedussi, B., Almasian, M., de Vos, J., VanBavel, E. & Bakker, E. N. Paravascular spaces at the brain surface: Low resistance pathways for cerebrospinal fluid flow. *J. Cereb. Blood Flow & Metab.* **38**, 719–726 (2018).
6. Tithof, J. *et al.* A network model of glymphatic flow under different experimentally-motivated parametric scenarios. *Iscience* **25** (2022).
7. Daversin-Catty, C., Gjerde, I. G. & Rognes, M. E. Geometrically reduced modelling of pulsatile flow in perivascular networks. *Front. Phys.* **10**, 882260 (2022).
8. Gjerde, I. G., Kuchta, M., Rognes, M. E. & Wohlmuth, B. Directional flow in perivascular networks: Mixed finite elements for reduced-dimensional models on graphs. *J. Theor. Biol.* (2024).
9. Ern, A., Stephansen, A. F. & Zunino, P. A discontinuous Galerkin method with weighted averages for advection–diffusion equations with locally small and anisotropic diffusivity. *IMA J. Numer. Analysis* **29**, 235–256 (2009).
10. Di Pietro, D. A. & Ern, A. *Mathematical aspects of discontinuous Galerkin methods*, vol. 69 (Springer Science & Business Media, 2011).
11. Quarteroni, A. & Quarteroni, S. *Numerical models for differential problems*, vol. 2 (Springer, 2009).
12. Hong, Q., Kraus, J., Xu, J. & Zikatanov, L. A robust multigrid method for discontinuous Galerkin discretizations of Stokes and linear elasticity equations. *Numer. Math.* **132**, 23–49 (2016).
13. Brezzi, F., Douglas, J., Durán, R. & Fortin, M. Mixed finite elements for second order elliptic problems in three variables. *Numer. Math.* **51**, 237–250 (1987).
14. Taylor, G. I. Dispersion of soluble matter in solvent flowing slowly through a tube. *Proc. Royal Soc. London. Ser. A. Math. Phys. Sci.* **219**, 186–203 (1953).
15. Watson, E. Diffusion in oscillatory pipe flow. *J. Fluid Mech.* **133**, 233–244 (1983).
16. Asgari, M., De Zélicourt, D. & Kurtcuoglu, V. Glymphatic solute transport does not require bulk flow. *Sci. reports* **6**, 38635 (2016).
17. Sharp, K. M., Carare, R. O. & Martin, B. A. Dispersion in porous media in oscillatory flow between flat plates: applications to intrathecal, periarterial and paraarterial solute transport in the central nervous system. *Fluids Barriers CNS* **16**, 1–17 (2019).
18. Ray, L. A., Pike, M., Simon, M., Iliff, J. J. & Heys, J. J. Quantitative analysis of macroscopic solute transport in the murine brain. *Fluids Barriers CNS* **18**, 55 (2021).
19. Troyetsky, D. E., Tithof, J., Thomas, J. H. & Kelley, D. H. Dispersion as a waste-clearance mechanism in flow through penetrating perivascular spaces in the brain. *Sci. reports* **11**, 4595 (2021).
20. Causemann, M., Vinje, V. & Rognes, M. E. Human intracranial pulsatility during the cardiac cycle: a computational modelling framework. *Fluids Barriers CNS* **19**, 84 (2022).
21. Balédent, O. Imaging of the cerebrospinal fluid circulation. *Adult hydrocephalus* **256**, 121 (2014).

22. Vinje, V. *et al.* Respiratory influence on cerebrospinal fluid flow – a computational study based on long-term intracranial pressure measurements. *Sci. Rep.* **9** (2019).

23. Gutiérrez-Montes, C. *et al.* Effect of normal breathing on the movement of CSF in the spinal subarachnoid space. *Am. J. Neuroradiol.* **43**, 1369–1374 (2022).

24. Liu, P., Owashi, K., Metanbou, S., Capel, C. & Balédent, O. Using real time phase contrast MRI to investigate CSF oscillations and aqueductal pressure gradients during free breathing. In *ISMRM 2024*, 1189 (2024).

25. van de Vosse, F. N. & van Dongen, M. Cardiovascular fluid mechanics. *Lect. notes* (1998).

26. Gjerde, I. G., Rognes, M. E. & Sánchez, A. L. The directional flow generated by peristalsis in perivascular networks—theoretical and numerical reduced-order descriptions. *J. Appl. Phys.* **134** (2023).

27. Eide, P. K. & Ringstad, G. Functional analysis of the human perivascular subarachnoid space. *Nat. Commun.* **15**, 2001 (2024).

28. Broggini, T. *et al.* Long-wavelength traveling waves of vasomotion modulate the perfusion of cortex. *Neuron* **112**, 2349–2367.e8 (2024).

29. Jung, J.-Y., Lee, Y.-B. & Kang, C.-K. Novel technique to measure pulse wave velocity in brain vessels using a fast simultaneous multi-slice excitation magnetic resonance sequence. *Sensors* **21**, 6352 (2021).

30. Hodneland, E. *et al.* A new framework for assessing subject-specific whole brain circulation and perfusion using MRI-based measurements and a multi-scale continuous flow model. *PLoS computational biology* **15**, e1007073 (2019).

31. Linninger, A. A. *et al.* Cerebrospinal fluid flow in the normal and hydrocephalic human brain. *IEEE Transactions on Biomed. Eng.* **54**, 291–302 (2007).

32. Sweetman, B. & Linninger, A. A. Cerebrospinal fluid flow dynamics in the central nervous system. *Ann. Biomed. Eng.* **39**, 484–496 (2011).

33. Hornkjøl, M. *et al.* CSF circulation and dispersion yield rapid clearance from intracranial compartments. *Front. Bioeng. Biotechnol.* **10**, 932469–932469 (2022).

34. Karki, P. *et al.* Real-time 2d phase-contrast MRI to assess cardiac-and respiratory-driven CSF movement in normal pressure hydrocephalus. *J. Neuroimaging* **35**, e70000 (2025).

35. Liu, P. *et al.* Transmantle pressure under the influence of free breathing: non-invasive quantification of the aqueduct pressure gradient in healthy adults. *Fluids Barriers CNS* **22**, 1 (2025).

36. Takizawa, K., Matsumae, M., Sunohara, S., Yatsushiro, S. & Kuroda, K. Characterization of cardiac- and respiratory-driven cerebrospinal fluid motion based on asynchronous phase-contrast magnetic resonance imaging in volunteers. *Fluids Barriers CNS* **14**, 25 (2017).

37. Yildiz, S. *et al.* Quantifying the influence of respiration and cardiac pulsations on cerebrospinal fluid dynamics using real-time phase-contrast MRI. *J. Magn. Reson. Imaging* **46**, 431–439 (2017).

38. Stockman, H. W. Effect of anatomical fine structure on the dispersion of solutes in the spinal subarachnoid space. *J. Biomech. Eng.* **129**, 666–675 (2007).

39. Hettiarachchi, H. D. M., Hsu, Y., Harris, T. J., Jr, Penn, R. & Linninger, A. A. The effect of pulsatile flow on intrathecal drug delivery in the spinal canal. *Ann. Biomed. Eng.* **39**, 2592–2602 (2011).

40. Ichimura, T., Fraser, P. A. & Cserr, H. F. Distribution of extracellular tracers in perivascular spaces of the rat brain. *Brain Res.* (1991).

41. Foley, C. P., Nishimura, N., Neeves, K. B., Schaffer, C. B. & Olbricht, W. L. Real-time imaging of perivascular transport of nanoparticles during convection-enhanced delivery in the rat cortex. *Ann. Biomed. Eng.* **40**, 292–303 (2012).

42. Schain, A. J., Melo-Carrillo, A., Strassman, A. M. & Burstein, R. Cortical spreading depression closes paravascular space and impairs glymphatic flow: Implications for migraine headache. *J. Neurosci.* **37**, 2904–2915 (2017).

43. Mestre, H. *et al.* Periarteriolar spaces modulate cerebrospinal fluid transport into brain and demonstrate altered morphology in aging and Alzheimer's disease. *Nat. Commun.* **13**, 3897 (2022).

44. Smets, N. G., van der Panne, S. A., Strijkers, G. J. & Bakker, E. N. T. P. Perivascular spaces around arteries exceed perivenous spaces in the mouse brain. *Sci. Rep.* **14**, 17655 (2024).

45. Raicevic, N. *et al.* Sizes and shapes of perivascular spaces surrounding murine pial arteries. *Fluids Barriers CNS* **20**, 56 (2023).

271 **46.** Vinje, V., Bakker, E. N. & Rognes, M. E. Brain solute transport is more rapid in periarterial than perivenous spaces. *Sci.*
272 *Reports* **11**, 1–11 (2021).

273 **47.** Tithof, J., Kelley, D. H., Mestre, H., Nedergaard, M. & Thomas, J. H. Hydraulic resistance of periarterial spaces in the
274 brain. *Fluids Barriers CNS* **16**, 19 (2019).

275 **48.** Boster, K. A., Sun, J., Shang, J. K., Kelley, D. H. & Thomas, J. H. Hydraulic resistance of three-dimensional pial
276 perivascular spaces in the brain. *Fluids Barriers CNS* **21**, 7 (2024).